

Statistical Power, the Bispectrum and the Search for Non-Gaussianity in the CMB Anisotropy

Nicholas G. Phillips

*Raytheon ITSS, Laboratory for Astronomy and Solar Physics, Code 685, NASA/GSFC,
Greenbelt, Maryland 20771*

and

A. Kogut

*Laboratory for Astronomy and Solar Physics, Code 685, NASA/GSFC, Greenbelt, Maryland
20771*

ABSTRACT

We use simulated maps of the cosmic microwave background anisotropy to quantify the ability of different statistical tests to discriminate between Gaussian and non-Gaussian models. Despite the central limit theorem on large angular scales, both the genus and extrema correlation are able to discriminate between Gaussian models and a semi-analytic texture model selected as a physically motivated non-Gaussian model. When run on the COBE 4-year CMB maps, both tests prefer the Gaussian model. Although the bispectrum has comparable statistical power when computed on the full sky, once a Galactic cut is imposed on the data the bispectrum loses the ability to discriminate between models. Off-diagonal elements of the bispectrum are comparable to the diagonal elements for the non-Gaussian texture model and must be included to obtain maximum statistical power.

Subject headings: cosmic microwave background — cosmology: observations — methods: statistical

1. Introduction

The statistics of the cosmic microwave background (CMB) probe physical conditions in the early universe. Most inflationary models predict the CMB to follow Gaussian statistics (Bardeen *et. al.* 1983; Guth and Pi 1982; Hawking 1982; Starobinskii 1982). Searching CMB data for non-Gaussian distributions is thus an important test of inflationary cosmologies. Recent analyses of the full-sky COBE data provide mixed results. Kogut *et. al.* (Kogut *et. al.* 1995; Kogut *et. al.* 1996) use a likelihood analysis to compare the COBE-DMR 2- and 4-year maps to the standard Gaussian model and a set of non-Gaussian toy models. The COBE data lie near the mode of the statistical distributions of the genus, 3-point correlation, and correlation of extrema points for the

Gaussian model, while rejecting several non-Gaussian alternatives. Other authors using similar statistics on the COBE maps find comparable results (Hinshaw *et al.* 1994; Smoot *et al.* 1994; Luo 1994; Torres *et al.* 1995; Colley *et al.* 1996; Heavens 1998). More recently, several authors have challenged the conclusion that the COBE data are well described by Gaussian statistics. Tests using the normalized bispectrum (Ferreira *et al.* 1998; Magueijo 2000) and a wavelet analysis (Pando *et al.* 1998) both show the COBE data to be incompatible with Gaussian simulations at 98% confidence; however, these analyses did not test any non-Gaussian alternatives. The recent work of Mukherjee (2000) brings into question the the statistical significance of the (Pando *et al.* 1998) result. In (Mukherjee *et al.* 2000) a proper Monte-Carlo estimation of the significance level shows the wavelet technique does not yield strong evidence for non-Gaussianity in the 4-year COBE data. Bromley and Tegmark (1999) argue that the non-Gaussian signal (if any) must lie in the *phase* information in the COBE sky maps, while Banday *et al.* (2000) ascribe the discrepancy to instrumental artifacts in one of the DMR frequency channels.

Searches for non-Gaussianity are complicated by several factors. On large angular scales, the superposition of multiple sources within the instrument angular resolution tends to push initially non-Gaussian distributions toward the Gaussian model (the Central Limit Theorem). Sample variance can occasionally produce a non-Gaussian distribution drawn from a Gaussian parent population. Given enough independent tests of the same observable sky, some outliers are expected (Bromley and Tegmark 1999). *Demonstrating that a statistic calculated for a CMB data set lying far from the mode expected for a Gaussian sky is a necessary but not sufficient condition to conclude that the data are not, in fact, a sample drawn from a Gaussian parent population.*

The statistical power of a test quantifies the probability of correctly accepting or rejecting hypotheses based on the results of that test. Quantifying the power for a given statistic thus requires at least two competing hypotheses. Since there is a single Gaussian distribution but an infinite number of non-Gaussian distributions, we must necessarily restrict the scope of specific non-Gaussian hypotheses. (Kogut *et al.* 1995; Kogut *et al.* 1996) used non-Gaussian toy models to show that the genus and extrema correlation could discriminate between Gaussian and non-Gaussian populations. We extend this analysis to include the bispectrum, replacing the earlier toy models with a model of topological defects as a specific example of a physically-motivated alternative to the standard Gaussian model.

2. Likelihood Analysis and Statistical Power

Maximum-likelihood techniques are a commonly used tool for statistical inference. Given any set of K statistics derivable from a sky map, which we view as the vector \mathbf{S} , we define

$$\chi^2(\mathbf{S}) = \sum_{\alpha, \beta=1}^K (S_\alpha - \langle S_\alpha \rangle) (\mathbf{M}^{-1})_{\alpha\beta} (S_\beta - \langle S_\beta \rangle) \quad (1)$$

where $\langle \mathbf{S} \rangle$ is the mean value of the statistic for the model under consideration, and \mathbf{M} its covariance matrix. The likelihood is then

$$\mathcal{L}(\mathbf{S}) = \frac{\exp(-\frac{1}{2}\chi^2)}{\sqrt{(2\pi)^K \det(\mathbf{M})}} \quad (2)$$

where we make the convenient assumption that the statistics \mathbf{S} obey a multivariate Gaussian probability distribution. Since the large-scale CMB anisotropy is close to a Gaussian distribution, We do not expect the calculation of the true distributions based on Monte-Carlo simulations can significantly change the relative statistical powers we determine. For the simple comparison of two models, we compute the likelihood functions \mathcal{L}_1 and \mathcal{L}_2 for a given statistic $\mathbf{S}(\Delta\mathbf{T})$. The data ΔT are more likely to be drawn from parent population model 1 if $\mathcal{L}_1(\mathbf{S}(\Delta T)) > \mathcal{L}_2(\mathbf{S}(\Delta T))$, and vice versa for model 2.

For a statistic to be useful, we need to determine how well it can discriminate between the models under consideration. Recall there are two types of error: a Type I error rejects a hypothesis when it is correct, while a Type II error accepts a hypothesis when it is false. The statistical power of a test quantifies the robustness of a test against Type II errors. By sampling the likelihood functions \mathcal{L}_i with independent samples drawn from each of the two models under consideration, we obtain the probability to incorrectly identify a sample from model i as drawn from model j : $P(\mathbf{S}_i|H_j)$, where \mathbf{S}_i is extracted from a realization of model i . $P(\mathbf{S}_1|H_1)$ is thus the probability to correctly identify a sample from model 1 under the hypothesis H_1 that it is from model 1, while $P(\mathbf{S}_2|H_1)$ is the probability to incorrectly identify a sample from model 2 under the same hypothesis. The probability to obtain the correct conclusion is thus

$$\Pi_i = \frac{P(\mathbf{S}_i|H_i)}{P(\mathbf{S}_1|H_i) + P(\mathbf{S}_2|H_i)}. \quad (3)$$

If the likelihood analysis of a CMB data set yields the conclusion that the data are drawn from model 1 and $\Pi_i \sim 1$, we can be confident we have made the correct conclusion. If $\Pi_i \sim \frac{1}{2}$ then no conclusions can be made concerning the result since we only have a 50-50 chance of being right.

3. Models

Any maximum likelihood analysis assumes the comparison of at least two competing models. We use three statistical tests (genus, extrema correlation, and bispectrum) of the COBE-DMR 4-year sky maps to compare a Gaussian model against a semi-analytic texture model, a physical non-Gaussian theory. We generate 1500 simulated sky maps for each model, and use these maps to generate the mean values $\langle S_\alpha \rangle$ and the covariance matrices

$$M_{\alpha\beta} = \frac{1}{N} \sum_i (S_\alpha^{(i)} - \langle S_\alpha \rangle)(S_\beta^{(i)} - \langle S_\beta \rangle), \quad (4)$$

including effects of instrument noise and Galaxy cut. We then generate an additional 1500 simulated sky maps of each of the models for a maximum-likelihood comparison, which we use to quantify the power of each statistical test.

The microwave anisotropy may conveniently be expressed as a sum of spherical harmonics, $\Delta T_i = \sum_{lm} a_{lm} Y_{lm}(\theta_i, \phi_i)$. For the Gaussian model, we randomly distribute the spherical harmonic coefficients as $a_{lm} = r \exp(i\delta)$, where δ is uniformly distributed between 0 and 2π and r a Gaussian random variable with zero mean and variance

$$\langle r^2 \rangle = \frac{4\pi}{5} (Q_{\text{rms}})^2 \frac{\Gamma(l + (n-1)/2) \Gamma((9-n)/2)}{\Gamma(l + (5-n)/2) \Gamma((3+n)/2)}. \quad (5)$$

We use the best-fit spectral index $n = 1.2$ from the COBE 4-year data (Bennett *et. al.* 1996; Górski *et. al.* 1996; Hinshaw *et. al.* 1996a; Wright *et. al.* 1996). Our results are insensitive to changes of $\delta n \pm 0.2$, roughly the uncertainty in the fitted index.

Our semi-analytic model is based on probability distributions for the texture energy density. We use numerical simulations of the texture field equations to derive these distributions and in turn use these distributions to generate simulated CMB anisotropy sky maps. The main addition to previous semi-analytic models (Turok and Spergel 1990) is the inclusion of partial wound events (Borril *et. al.* 1994). In (Phillips and Kogut 1995), it was verified that these events, though less energetic than the unwinding events considered in (Turok and Spergel 1990), are more numerous. When they are included, the number of free parameters of the texture model increases from just the symmetry breaking scale to now include the minimum and maximum strengths of the partial wound events. As we discuss in the Appendix we take the maximum strength to be the same as the unwinding strength, since these are topological configurations that just barely become knots. The minimum strength is put at 1/4 the maximum. Our results are insensitive to the precise value chosen.

We smooth each realization of a theory sky map with a Gaussian profile of 7° FWHM to account for the COBE-DMR beam profile. We add a pixel-wise noise to each map, $T_i^{\text{instr}} = AT_i + n_i$, using the noise template appropriate for the 4-year COBE data as corrected for Galactic emission using either the “correlation” or “linear combination” models of (Hinshaw *et. al.* 1996b). All statistics are evaluated only for the high-latitude sky (3881 pixels at $|b| > 20^\circ$ with custom cutouts near Ophiuchus and Orion, (Bennett *et. al.* 1996; Banday *et. al.* 1996)) from which a fitted dipole and quadrupole have been removed.

4. Genus

The statistical properties of the CMB can be characterized by the excursion regions enclosed by isotherm contours. The genus is the total curvature of the contours at fixed temperature, and may loosely be defined as the number of isolated high temperature regions (hot spots) minus the number of isolated low temperature regions (cold spots) (Gott *et. al.* 1990). The genus per unit area is a locally invariant quantity and is insensitive to incomplete sky coverage (e.g. removal of the Galactic plane).

We use a nearest-neighbor search to count the number of isolated hot and cold spots separated

by temperature threshold ν . For each map, we compute the genus at 31 values from $\nu = -3\sigma$ to $\nu = +3\sigma$, where $\sigma = \sqrt{\langle \Delta T^2 \rangle}$ is the standard deviation of the noisy map. These values form the vector \mathbf{S} in the likelihood analysis. We adopt the difference in spot number as an estimate of the genus and use the Monte Carlo simulations to calibrate any difference induced by the Galactic cut between this definition and the total curvature. The two definitions are identical in the absence of a Galactic cut, and the nearest-neighbor algorithm allows significant computational savings.

We use the genus to do a maximum likelihood fit for the model amplitude for the COBE data. We find that both models yield similar amplitudes, $A_{\text{fit,Gauss}} = 0.64$ ($Q_{\text{rms}} = 13.0 \mu K$) and $A_{\text{fit,texture}} = 0.62$ ($G\eta^2 = 3.5 \times 10^{-7}$). The likelihood of the COBE data is greater for the Gaussian model. To derive the statistical power for the genus, we present the likelihood functions with 1500 independent sampling maps, with amplitudes ranging from $A = 0$ to $A = 3$ in 31 uniform steps. We fit each sample for the amplitude, then select the more likely model. We then filter these samples to have an amplitude close to the fitted DMR map: $|A_{\text{fit}} - A_{\text{fit,Gauss}}| \leq 0.05$ (The filter width corresponds to our sampling interval in A ; our results for Π_i are insensitive to the exact value). We compare the number of input models identified as each model (Table 1). We obtain $\Pi_{\text{Gauss}} = 990/(990 + 704) = 58\%$. Although the Gaussian model is the more likely model for the COBE data, we can not be overconfident about this result. When the noisier “combination” map is used, the statistical power drops to $\Pi_{\text{Gauss}} = 51\%$ and $\Pi_{\text{Texture}} = 54\%$. Table 2 shows the statistical power for the various statistical tests.

5. Extrema Correlation

The extrema (peaks and valleys) of a field are defined as those points with $\nabla T = 0$. For a pixelized map, this reduces to the collection of pixels hotter or colder than all of their nearest neighbors. Identifying pixels hotter than their neighbors produces a set of “peaks”, while the locally coldest pixels produce the “valleys”.

The number density of peaks or valleys is dominated by the noise properties of the map (Kogut *et. al.* 1995). The clustering of the extrema, as measured by the 2-point correlation function of the maxima and minima, provides additional information on the underlying CMB temperature field. We define the extrema correlation function as the 2-point function of all extrema points,

$$C_{\text{ext}}(\theta) = \frac{\sum_{i,j} w_i w_j T_i T_j}{\sum_{i,j} w_i w_j}$$

(Kogut et al. 1995), where the sum over pixel temperatures is restricted to the set of maxima and minima pixels separated by θ evaluated on the cut sky. Since the correlation properties of the non-uniform noise in the DMR maps are different from the underlying CMB temperature field, we smooth the maps with an additional 7° FWHM Gaussian prior to collating the extrema as a compromise between suppressing noise and removing CMB power at small scales, as was pointed out in (Kogut *et. al.* 1995).

The clustering of extrema depends on the threshold ν , as defined for the genus. We evaluate $C_{\text{ext}}(\theta)$ at thresholds $|\nu| = 0, 1, \text{ and } 2$. Since, by definition, two peaks can not be adjacent, we ignore both the bin at zero angular separation and the first non-zero bin in all subsequent analysis. Simulations show that the results are dominated by the first few remaining bins; consequently, we speed processing by truncating the correlation function at separation $\theta = 60^\circ$ for a total of 20 angular bins of 3° per bin at each of the three thresholds. We concatenate the three binned extrema correction functions together to form our vector \mathbf{S} for the likelihood analysis. A maximum-likelihood analysis of the COBE 4-year data shows the Gaussian model to be modestly more likely than the texture model. The statistical power of the extrema correlation is comparable to the genus (Table 2).

6. Bispectrum

A third way to characterize a random field is its hierarchy of n point functions. Since a Gaussian random field is completely characterized by its one and two point functions, the three point function or its harmonic conjugate, the bispectrum, may prove sensitive to non-Gaussian features in the data. We assume that the three point function only depends on the angular separation between points,

$$C^{(3)}(\theta_{12}, \theta_{13}, \theta_{23}) = \langle \Delta T(\mathbf{n}_1) \Delta T(\mathbf{n}_2) \Delta T(\mathbf{n}_3) \rangle, \quad (6)$$

where $\cos \theta_{ij} = \mathbf{n}_i \cdot \mathbf{n}_j$. The expansion in terms of Legendre polynomials (Gangui *et. al.* 1994) is given by

$$\begin{aligned} C^{(3)}(\theta_{12}, \theta_{13}, \theta_{23}) &= \sum_{l_1, l_2, l_3} \sum_{m_1, m_2, m_3} \frac{2l_1 + 1}{4\pi} \frac{2l_2 + 1}{4\pi} \frac{2l_3 + 1}{4\pi} B_{l_1 l_2 l_3}^{m_1 m_2 m_3} \\ &\times \sum_{j, k, l} \sum_{m_j, m_k, m_l} P_j(\theta_{12}) P_k(\theta_{13}) P_l(\theta_{23}) \mathcal{H}_{j l l_1}^{m_j m_l m_1} \mathcal{H}_{k j l_2}^{m_k m_j m_2} \mathcal{H}_{k l l_3}^{m_k m_l m_3} \end{aligned} \quad (7)$$

with

$$\mathcal{H}_{l_1 l_2 l_3}^{m_1 m_2 m_3} = \int Y_{l_1 m_1}^*(\mathbf{n}) Y_{l_2 m_2}(\mathbf{n}) Y_{l_3 m_3}(\mathbf{n}) .d\mathbf{n} \quad (8)$$

The bispectrum expansion coefficients are defined in terms of the spherical expansion coefficients a_{lm} via

$$B_{l_1 l_2 l_3}^{m_1 m_2 m_3} = a_{l_1 m_1} a_{l_2 m_2} a_{l_3 m_3}. \quad (9)$$

Our assumption that $C^{(3)}$ depends only on the angular separation θ_{ij} implies we are working with an isotropic cosmology. This leads us to consider the angular averaged bispectrum coefficients

$$B_{l_1 l_2 l_3} = \sum_{m_1, m_2, m_3} \begin{pmatrix} l_1 & l_2 & l_3 \\ m_1 & m_2 & m_3 \end{pmatrix} B_{l_1 l_2 l_3}^{m_1 m_2 m_3} \quad (10)$$

where (\dots) are the Wigner 3-j symbols. We also introduce the normalized coefficients

$$I_{l_1 l_2 l_3}^3 = \alpha_{l_1 l_2 l_3} \frac{|B_{l_1 l_2 l_3}|}{(C_{l_1} C_{l_2} C_{l_3})^{\frac{1}{2}}} \quad (11)$$

$$\alpha_{l_1 l_2 l_3} = \frac{1}{(((2l_1 + 1)(2l_2 + 1)(2l_3 + 1))^{\frac{1}{2}})} \begin{pmatrix} l_1 & l_2 & l_3 \\ 0 & 0 & 0 \end{pmatrix}^{-1}$$

The diagonal ($l_1 = l_2 = l_3 = l$) coefficients are the I_l^3 coefficients of (Ferreira *et. al.* 1998) while the J_l^3 coefficients of (Magueijo 2000) correspond to $l_1 = l - 2$, $l_2 = l$ and $l_3 = l + 2$.

To compute the bispectrum coefficients for our likelihood analysis, we fit the spherical expansion coefficients a_{lm} on the cut sky up to a maximum value l_{\max} . We use these best fit a_{lm} to construct the bispectrum coefficients (10) and form the vector $\mathbf{S} = \{I_{lll}^3\}_{l=2,4,\dots,l_{\max}}$. With this choice, our likelihood analysis uses the same statistic as (Ferreira *et. al.* 1998) and we find there is no statistical power: $\Pi_{I_l^3, \text{Gauss}} = \Pi_{I_l^3, \text{texture}} = 50\%$. Ferreira *et. al.* (1998) used $l_{\max} = 18$; we find no change in statistical power as l_{\max} is increased to 30. We find a similar lack of power using $\mathbf{S} = \{|B_{lll}|\}$. We conclude that neither the bispectrum nor the normalized bispectrum in this form can differentiate between Gaussian and texture models, even though these models have statistically identifiable differences in the genus and extrema correlation.

There are two possible explanations for this failure: i) the galaxy cut is aliasing too much power; or ii) we are not using enough of the available information present in the bispectrum. To address these possibilities, we vary both the size of the galaxy cut and the number of the off-diagonal terms of the bispectrum. For a statistical isotropic field, the two-point function has no coupling between different l multipoles: $\langle a_{lm} a_{l'm'}^* \rangle = C_l \delta_{ll'} \delta_{mm'}$. We find this assumption can not be made for the three point function. Figure 1a shows the distribution of $\langle |B_{l_1 l_2 l_3}| \rangle$ values for an $n = 1$ Gaussian model without noise or a galaxy cut (averaged over 1500 realizations). The diagonal values, $\langle |B_{lll}| \rangle$, are dominant, but the off-diagonal terms also have non-zero values comparable to the diagonal. Moreover, the values group according to how much they are off the diagonal. There are three groups: the diagonal values, the terms off just one diagonal ($\langle |B_{ll,l' \neq l}| \rangle$), and finally the terms completely off the diagonal¹ ($\langle |B_{l_1 l_2 l_3}| \rangle$, $l_1 \neq l_2 \neq l_3$). Figure 1b shows the distribution for our texture model. The bispectrum coefficient values still cluster, but not as tightly as the Gaussian model. The J_l^3 coefficients of (Magueijo 2000) are in this last group. Their choice of statistic misses the more significant set of terms off just one diagonal. The normalized bispectrum coefficients $\langle I_{l_1 l_2 l_3}^3 \rangle$ demonstrate similar clustering properties.

The Galactic cut destroys the bispectrum's ability to differentiate models. Figures 1c and 1d show the distributions of $\langle |B_{l_1 l_2 l_3}| \rangle$ for Gaussian and texture models after a galaxy cut is included. The values no longer cluster, and are no longer identifiable by model. The spherical harmonics Y_{lm} are no longer orthogonal on the cut sky; the resulting aliasing of power between modes overwhelms

¹We only consider the terms that are not forced to zero by the triangularity of the 3-j symbols.

the signal.

To quantify this failure, we compute the statistical power as we impose the simple latitudinal cut of removing pixels with $\theta \leq b$, for b varying from 0° to 14° . We set a signal amplitude that corresponds to the genus and extrema correlation function ($A = 0.64$). Since the bispectrum computed using only the diagonal values never shows statistical power, we include both the diagonal and once-off-the-diagonal terms (the two rightmost groups in Fig 1). Figure 2 shows that the probability to correctly identify the input model falls monotonically as the Galactic cut is increased. For comparison purposes, we also plot the statistical power for the genus, which shows only a slight trend consistent with larger sample variance as the solid angle available for analysis is reduced. With no galactic cut, the bispectrum has comparable power as the genus². The statistical power of the bispectrum drops steadily until cut $b < 12^\circ$, where there is no power. The normalized bispectrum $I_{ll'}^3$ is *never* able to differentiate between the models, even when there is no galaxy cut present.

The other important consideration is how much information is needed. For $l_{\max} = 20$, there are 770 nonzero, unique bispectrum values, of which 10 are the non-zero diagonal values. Using all values instead of just the diagonal values is computationally expensive. We use instead the diagonal terms and terms with one off-diagonal l value (second group from the right in Figure 1) to form the vector $\mathbf{S} = \{|B_{ll'}|\}$. The restriction $|l - l'| \leq \Delta l$ selects how many of the off-diagonal terms we use. $\Delta l = 0$ corresponds to the analysis of (Ferreira *et. al.* 1998) and $\Delta l = l_{\max}$ includes all the once-off-the-diagonal terms. Figure 3 shows the statistical power of the bispectrum as we increase Δl , where we consider both noisy and noiseless data sets evaluated over the full sky. The power is greater without noise; the statistical power of the Gaussian model is fairly constant after the inclusion of just a few extra off-diagonal terms. For the texture mode, the inclusion of additional off-diagonal terms steadily improves the probability for correct identification until $\Delta l \sim l_{\max}/2$. With noise, the statistical power for either model levels out at about the same value as the genus and extrema correlation function. This suggests that but for the need to include a galaxy cut, a likelihood analysis based on $|B_{ll'}|$ would be as powerful as the other tests. The galaxy cut aliases power in the conjugate harmonic space, but has negligible effect in the coordinate space used by the genus and extrema correlation function.

The addition of off-diagonal terms is important for the non-Gaussian texture model. For ideal (noiseless) data, the probability to correctly identify the texture model goes from 59% for only diagonal terms to 74% when all $|B_{ll'}|$ terms are considered. In contrast, the probability to correctly identify the Gaussian model is nearly constant. Since the three point function contains no new information for a Gaussian theory, we do not expect much improvement in the Gaussian model as the number of terms is increased. The texture model was chosen exactly because it is an example of a non-Gaussian theory, so the three point function or bispectrum should be sensitive to the gradual addition of the information present in the off-diagonal terms.

²Since we fix the input amplitude instead of fitting, the genus power here is slightly larger than shown in Table 2.

We have duplicated all the analysis discussed above for the normalized bispectrum coefficients $I_{ll'}^3$ introduced by (Ferreira *et. al.* 1998). Figs 2 and 3 show the likelihood analysis in terms of the normalized bispectrum never has any statistical power. For the ideal situation of noiseless data without a galaxy cut, the probability to correctly identify either model is at best 52%. The statistic J_l^3 of (Magueijo 2000) corresponds to our $I_{l-2,l,l+2}^3$ and is thus not directly covered in our analysis. Figures 1a and 1b show J_l^3 to be of lesser significance than our most general set of $I_{ll'}^3$'s and we can not expect any statistical power for this choice. Although we have tested only a single non-Gaussian model, the normalized bispectrum does not appear to be a promising test of the statistical distribution of CMB anisotropy.

7. Discussion.

Recent work has generated new interest in statistical tests of the CMB. Comparison of the bispectrum of the COBE-DMR 4-year sky maps to simulations of Gaussian maps show the COBE data to lie far from the mode of the Gaussian models (Ferreira *et. al.* 1998). Since this work tested only Gaussian models, it is not clear whether the discrepant values result from non-Gaussian signals in the data (including instrumental artifacts) or are simply an outlier drawn from a Gaussian parent population. We compute the statistical power of several popular statistics (the genus, extrema correlation, and bispectrum) to determine their ability to distinguish between a Gaussian model and a texture model chosen as a physically motivated non-Gaussian alternative.

Both the genus and extrema correlation successfully discriminate between the models with 60% confidence, limited by the similarity of the texture model to a Gaussian on large angular scales (the central limit theorem). The COBE 4-year data prefer the Gaussian model, although the modest statistical power prevents a strong rejection of this specific non-Gaussian alternative. In contrast, we find that the bispectrum has no power to discriminate between models, and trace this to the aliasing of power caused by the Galactic cut imposed on the data. The normalized bispectrum *never* has any power, even run on noiseless simulations with no Galactic cut. Since the results presented in (Ferreira *et. al.* 1998) and (Magueijo 2000) are based on an analysis in terms of the normalized bispectrum, the results, though correct, have no statistical power. Their results provide a necessary, but not sufficient, condition to rule out an underlying Gaussian character to the CMB anisotropy.

The problem of aliased power can in principle be solved, either by windowing the multipole coverage or by construction of an explicitly orthogonal basis. With this in mind, we further explore the statistical power of the bispectrum using full sky coverage to avoid the problem of aliased power. We find significant coupling between multipoles in the bispectrum coefficients for the non-Gaussian (texture) model. Failure to include these off-diagonal terms reduces the statistical power of the bispectrum on the full sky from 67% (comparable to the genus or extrema correlation) to 55% (not much better than random guessing). The off-diagonal elements are more important for the non-Gaussian model, pointing out the importance of testing various statistics against some alternative

to the standard Gaussian model.

Appendix

A. Texture Model

In order to test the power of different statistics, we need an alternative hypothesis to the standard Gaussian model. Defect models (Kibble 1985a; Kibble 1985b; Vilenkin and Shellard 1995) are the only known cosmological alternatives expected to provide a significant non-Gaussian signal. Characterizing this non-Gaussian signal requires many realizations of the model. Unfortunately, the non-linear nature of defect models make it impossible to carry out the analysis in closed form, while also making exact numerical work computationally expensive. We use exact simulations of a texture model to derive statistical descriptions of the energy density, then use these statistical descriptions to rapidly generate additional realizations of the model.

Textures (Turok 1989) are a class of topological defects in which the vacuum manifold of the order field in broken symmetric phase is of the same dimension as the spatial geometry. This allows the order field to remain on the vacuum manifold, regardless of initial conditions. Perturbations in the energy density are driven solely by the order field’s kinetic energy. As the correlation length of the order field grows, causal regions emerge that possess non-trivial topological charge (knots). These configurations collapse until the energy density is great enough for the order field to tunnel through the vacuum manifold and unwind. As CMB photons travel through these evolving regions of increased energy density, they become blue/red shifted and the anisotropy arises. This basic picture of knots in the texture order field led to the first approximation of Turok and Spergel (1990) which randomly placed idealized knots across the sky. The resulting CMB anisotropy, however, did not agree with results derived from full numerical simulations (Pen *et. al.* 1994).

Borril *et. al.* (1994) suggested the existence of a less energetic but more numerous configuration: partially wound events (PWEs), in which order field wraps around the vacuum manifold but not enough to be knotted. In (Phillips and Kogut 1995), we directly verified, for an expanding flat universe, that PWEs are far more numerous than knots and that their contribution dominates the CMB anisotropy. In this Appendix, we provide a statistical description of the PWEs. We then extend the model of (Turok and Spergel 1990) by randomly placing texture events on the microwave sky, drawing each event from the correct distribution in energy.

A.1. Field Equations and Numerical Implementation

Since we are interested in times long after the phase transition for the order field, we treat the field as classical. Except for the special case where the field unwinds, we restrict the field to lie on the vacuum manifold. We will focus solely on textures, so the (real-valued) global order becomes $\tilde{\Phi} = (\tilde{\Phi}_1, \tilde{\Phi}_2, \tilde{\Phi}_3, \tilde{\Phi}_4)$ and the vacuum manifold is the three sphere S^3 : $|\tilde{\Phi}|^2 = \phi_0$. After re-scaling

the field $\Phi = \tilde{\Phi}/\phi_0$, the field dynamics are determined by the action

$$S[\Phi] = \int d^4x \sqrt{-g} \left[\frac{1}{2} (\partial_\mu \Phi) \cdot (\partial^\mu \Phi) - \lambda (|\Phi|^2 - 1) \right]. \quad (\text{A1})$$

The constraint that the field stay on the vacuum manifold is imposed via the Lagrange multiplier λ . This is the nonlinear σ model (NLSM) (see e.g. (Pen *et. al.* 1994)). We carry out our work for a spatial flat Robertson-Walker homogeneous universe. For this choice the field equations become

$$\ddot{\Phi} + 2\frac{\dot{a}}{a}\dot{\Phi} - \nabla^2 \Phi = \left(|\nabla \Phi|^2 - |\dot{\Phi}|^2 \right) \Phi \quad (\text{A2})$$

where $\dot{\Phi} = \partial\Phi/\partial\tau$ and $\nabla\Phi = \partial\Phi/\partial x_i$ is the spatial gradient. We refer the reader to (Phillips and Kogut 1995) for details of the derivation of discrete versions of these equations and their numerical implementation.

We characterize the field dynamics using two quantities. The first is the energy density, the $\tau\tau$ component of the field stress tensor:

$$\rho_{i,n} = \frac{1}{2} \left(|\dot{\Phi}_{i,n}|^2 + |\nabla\Phi_{i,n}|^2 \right) \quad (\text{A3})$$

with the obvious discrete versions of the derivatives, where index i labels the spatial grid cells and t is the temporal label. The second quantity is the cell alignment,

$$\alpha_i = \left(\frac{1}{6} \sum_j \Phi_j \right) \cdot \Phi_i \quad (\text{A4})$$

where j runs over cell i 's six nearest neighbors. With this definition, the alignment of a grid cell is the cosine of the angle between the field configuration at i and the average of the field over i 's nearest neighbors. α_i measures how close the vacuum at i is to its neighbors, or how aligned the cell is with the local choice of vacuum. This gives a rough measure of the local topological charge (see (Borril 1995) for further discussion). According to this use of the NLSM model, knots are numerically identified by $\alpha_i < 0$ (Pen *et. al.* 1994). They are unwound by flipping the field to its anti-podal: $\Phi_i \rightarrow -\Phi_i$.

We base our analysis on a catalogue of events identified in 4000 simulations of the order field dynamics. The expansion scale factor $a(t)$ corresponds to a matter-dominated universe. We run the simulations on a 64^3 grid array with periodic boundary conditions, continuing until the horizon crossing time ($\Delta\tau = 32$). The initial order field configuration $\Phi(\mathbf{x}, \tau_0)$ is uniformly distributed over the vacuum manifold. We begin the simulation by integrating this initial random configuration, but with the anti-podal flipping of knot configurations disabled. This acts to “smooth” the initial order field while maintaining the constraint $|\Phi|^2 = 1$. We then re-enable the anti-podal unwinding and begin the event identification procedure outlined below.

A.2. Event Identification

As the casual horizon grows and regions of different vacua come into contact, the order field $\Phi(\mathbf{x})$ changes until it is in the same vacuum throughout. As this takes place the energy density due to the field rises. The dynamics of Φ force the region containing the changing Φ to shrink in size (Derrick 1964). When the total topological charge contained in this region is non-trivial, i.e., a knot, the energy density within the shrinking region will increase until the field can tunnel through the vacuum manifold and unwind the topological charge. The other possibility is that the order field within the region, though needing to resolve which vacuum the region will occupy, has no net topological charge. These are the partially wound events. They too are shrinking regions of growing energy, but now order field sorts itself out without having to tunnel through the vacuum manifold. In either case, after the region shrinks and resolves which vacuum to occupy, the region then expands as the stress energy diminishes.

We use this behavior to identify events in the numerical simulations. At each time step, we record the position, alignment, and energy density for each local maximum in the energy density, then track the spatial movement of each local maximum from one time step to the next. These local maxima are the grid centers of the growing/shrinking regions discussed above. We identify 300597 events in the 4000 simulations run. Figure 4 shows the temporal evolution of typical events. The alignment decreases and the energy increases as the texture becomes increasingly wound. Shortly after the alignment reaches a minimum, the energy density begins to decrease and the event dissipates.

Fig. 5 shows the distribution of these events sorted by the minimum alignment α_{\min} of each event. Three groupings are evident: knots, PWEs and noise. The knots are all events with minimum alignment less than zero. We identify all events with $\alpha_{\min} > 0.55$ as noise, since they have negligible contribution to the energy of the field. We identify all remaining events, $0 < \alpha_{\min} \leq 0.55$, as partially-wound events. With this identification, 4% of the events are knots, 56% are PWEs, and 40% are noise.

A.3. Partially Wound Event Distributions.

A semi-analytic model for textures requires a statistical description of the temporal and energy distribution for the PWEs. Instead of working directly with the energy distribution, we consider the alignment of the PWEs. The alignment is more closely related to the topological properties of the theory and as such is less sensitive to noise in the simulated order field.

We label each event by the minimum of its alignment, α_{\min} , and the conformal time τ_{\min} of this minimum alignment. Binning the PWEs according to α_{\min} and τ_{\min} shows the distribution to be separable, $dN_{\text{PWE}}(\alpha, \tau) \propto dN_1(\tau) dN_2(\alpha)$. Not surprisingly, the temporal distribution for the

PWEs has the same behavior as that for the knots,

$$dN_1(\tau) = \frac{\kappa_{PWE}}{\tau^4} d\tau; \quad \kappa_{PWE} = \frac{3}{5}. \quad (\text{A5})$$

We determine κ_{PWE} by comparing the total number of PWEs ($N_{PWE} = 168307$) to the number knots ($N_{\text{knot}} = 11295$). There are 15 partially wound events for each unwinding event.

Figure 6 shows the distribution in alignment, $dN_2(\alpha)$. The shape is well described by a χ^2 distribution with 4 degrees of freedom,

$$dN_2(\alpha) = A [\chi_\nu^2(x) + p_0] \quad (\text{A6})$$

where $\chi_\nu^2(x)$ is the χ^2 distribution for $\nu = 4$ degrees of freedom,

$$x = \frac{\bar{\alpha} - \alpha}{m}, \quad (\text{A7})$$

$\bar{\alpha} = 0.55$ is the alignment noise cutoff, and A is a normalization constant. The uncertainty in the number of events N_j in each bin is given by counting statistics, $\sigma_{N_j}^2 = N_j$. We thus fit the binned data to determine values

$$m = 0.165 \pm 0.003 \quad \text{and} \quad p_0 = 0.026 \pm 0.005 \quad (\text{A8})$$

A four-parameter fit with ν and $\bar{\alpha}$ free yields fitted values $\nu = 4.01 \pm 0.02$ and $\bar{\alpha} = 0.54 \pm 0.01$, justifying the choice of functional form of the probability distribution.

We also test the spatial properties of the partially-wound events, to determine whether one PWE will suppress or enhance the probability to find another PWE in the local neighborhood. The two-point correlation function for all PWEs is indistinguishable from one derived for the same number of events uniformly distributed in space. A principal moment analysis of the spatial distribution of the energy density around the grid center shows the PWEs to be spherically symmetric.

A.4. Sky Map Generation

Our semi-analytic model uses this statistical description of the order field in texture cosmologies to generate maps of simulated CMB anisotropy without requiring computationally expensive numerical simulation of the evolving order field. It extends the work of Turok and Spergel (1990) to include the more numerous partially-wound events. As in that work, we generate a random set of spherically symmetric events with uniform spatial distribution and τ^{-4} temporal distribution. Now, however, the energy of each event is drawn either from a mono-energetic knot population (6% probability) or from the distribution of PWEs (94% probability).

Deriving a map of the CMB anisotropy from a realization of random texture events requires fixing the relation between the minimum alignment α used to generate the PWE distribution (Eq.

A6) and the amplitude $\Delta T/T$ of the CMB anisotropy. Analysis of the simulations indicates this relation to be linear. Due to the discrete anti-nodal flipping algorithm, the energy scale of the *knots* in the simulations is arbitrary. We thus require two normalization parameters to fully specify CMB anisotropy given a distribution of texture events: the minimum and maximum energy of the PWEs relative to the knots. We take the maximum amplitude for PWEs to be equal to the amplitude for the knots: these represent (rare) events that just barely missed unwinding ($\alpha \sim 0$). The noise cutoff $\alpha_{\min} = 0.55$ provides a lower limit to the energy of PWEs used in the model; we thus take the minimum amplitude to be half way between the knot amplitude and zero.

A single realization of a CMB map using the semi-analytic model thus requires the following steps:

- 1) we compute the number of events in the observed universe by taking the product of the observed volume and the integrated temporal distribution (A5);
- 2) we distribute these events uniformly in space and with a τ^{-4} temporal distribution;
- 3) letting 6% of these be knots, we assign them the maximum amplitude and let the other 94% be PWEs. For the PWEs, we select random alignments from the distribution (A6) and linearly map to amplitudes as outlined above;
- 4) we use the result from (Turok and Spergel 1990) for the $\Delta T/T$ contribution to determine which pixels are influenced by each event.

We are thus left with one undetermined parameter, the amplitude of the knotted configurations. A single full-sky realization of the semi-analytic model with 6144 pixels requires only 20 seconds of CPU time on a Sun Ultra workstation at 360 MHz clock speed, achieving the goal of rapidly generating a large number of sky maps.

We thank Ue-Li Pen for valuable discussions. This work was funded in part through NASA RTOP 399-20-61-01.

REFERENCES

- Banday, A. J., *et al.* 1996, ApJ, 475, 393
- Banday, A. J., Zaroubi, S. and Górski, K. M. 2000, ApJ, 533, 575
- Bardeen, J. M., Steinhardt, P. J. and Turner, M. S. 1983, Phys. Rev. D, 28, 679
- Bennett, C. L., *et al.* 1996, ApJ, 464, L1
- de Bernardis, P., *et al.* (Boomerang Coll.) 2000, Nature, 404, 955
- Borril, J., *et al.* 1994, Phys. Rev. D, 50, 2469
- Borril, J. 1995, Phys. Rev. D, 50, 3676

- Bromley, B. C. and Tegmark, M. 1999, ApJ, 524, L79
- Colley, W. N., Gott Jr., J. R. and Park, C. 1996, MNRAS, 281, L82
- Derrick, G. H. 1964, J. Math. Phys., 5, 1252
- Ferreira, P. G., Magueijo, J. and Górki, K. M. 1998, ApJ, 503, L1
- Gangui, A., *et. al.*, ApJ, 430, 447
- Górski, K., *et. al.* 1996, ApJ, 464, L11
- Gott, J.R., Park, C., Juskiwicz, R., Biew, W.E., Bennett, D.P, Bochet, F.R., & Stebbins, A. 1990, ApJ, 352, 1
- Guth, A. and Pi, Y-S. 1982, Phys. Rev. Lett., 49, 1110
- Hawking, S. 1982, Phys. Lett., 115B, 295
- Heavens, A. F. 1998, MNRAS, 299, 805
- Hanany, S., *et. al* (Maxima Coll.) 2000, ApJ, submitted
- Hinshaw, G., *et. al.* 1994, ApJ, 431, 1
- Hinshaw, G., *et. al.* 1996, ApJ, 464, L17
- Hinshaw, G., *et. al.*, 1996, ApJ, 464, L25
- Kibble, T. W. B. 1985, Nucl. Phys. B, 262, 227
- Kibble, T. W. B. 1985, Nucl. Phys. B, 261, 750(E)
- Kogut, A., *et. al.* 1995, ApJ, 439, L29
- Kogut, A., *et. al.* 1996, ApJ, 464, L29
- Luo, X. 1994, Phys. Rev. D, 49, 3810
- Magueijo, J. 2000, ApJ, 528, L57
- MAP, see <http://www.map.gsfc.nasa.gov>
- Mukherjee, P., Hobson, M.P. and Lasenby, A. N. 2000, MNRAS submitted; astro-ph/0001385
- Pando, J., Valls-Gabaud, D. and Fang, L.-Z. 1998, Phys. Rev. Lett., 81, 4568
- Pen, U.-L., Spergel, D. and Turok, N. 1994, Phys. Rev. D, 47, 692
- Phillips, N. G. and Kogut, A. 1995, Phys. Rev. Lett., 75, 1264

Planck, see <http://sci.esa.int/home/planck/>

Starobinskii, A. A. 1982, Phys. Lett., 117B, 175

Smoot, G. F., *et al.* 1994, ApJ, 437, 1

Torres, S., *et al.* 1995, MNRAS, 274, 853

Turok, N. 1989, Phys. Rev. Lett., 63, 2625

Turok, N. and Spergel, D. 1990, Phys. Rev. Lett., 64, 2736

Vilenkin, A. and Shellard, E. P. S. 1995, Cosmic Strings and Other Topological Defects (Cambridge University Press: Cambridge)

Wright, E. L., *et al.* 1996, ApJ, 464, L21

Fig. 1.— Distribution of average bispectrum values $\langle |B_{l_1 l_2 l_3}| \rangle$ for 1500 maps. (a) Noiseless $n = 1$ Gaussian model, no galaxy cut. (b) Noiseless $E_{\min} = 0.25 E_{\max}$ texture model, no galaxy cut. (c) Same as (a), but now with a galaxy cut. (d) Same as (b), but now with a galaxy cut. (For ease of viewing, each of the bispectrum was rescaled to a common range. All analysis was done without this rescaling.)

Fig. 2.— Dependence of the statistical power of the bispectrum $|B_{l_1 l_2 l_3}|$ and power-spectrum normalized version $I_{l_1 l_2 l_3}^3$ on the size b of the galactic cut. The statistical power is measured by the probability to correctly identify the input model.

Fig. 3.— Statistical power of the bispectrum $|B_{ll'l'}|$ and normalized bispectrum $I_{ll'l'}^3$ as a function of the number of off-diagonal terms. The number of off-diagonal terms is controlled by the restriction $|l - l'| \leq \Delta l$. $\Delta l = 0$ uses only the diagonal terms and is appropriate only if there is no coupling between multipole terms in the bispectrum. The texture model (triangles) has significant contribution from off-diagonal terms. The normalized bispectrum has no power regardless of the number of off-diagonal terms.

Fig. 4.— Temporal evolution of typical texture events. The top panel shows the alignment at the center of each event at each time step. The bottom panel shows the energy density at the center, defined as the local maximum of the energy density.

Fig. 5.— Distribution of texture events sorted by the minimum alignment reached over the history of each event. Three peaks are evident. Events with $\alpha_{\min} < 0$ correspond to knots. The energy density at the time of minimum alignment (bottom panel) shows that the region $\alpha_{\min} > 0.55$ contributes negligible. We identify these events as noise. The middle region corresponds to partially-wound events (PWEs).

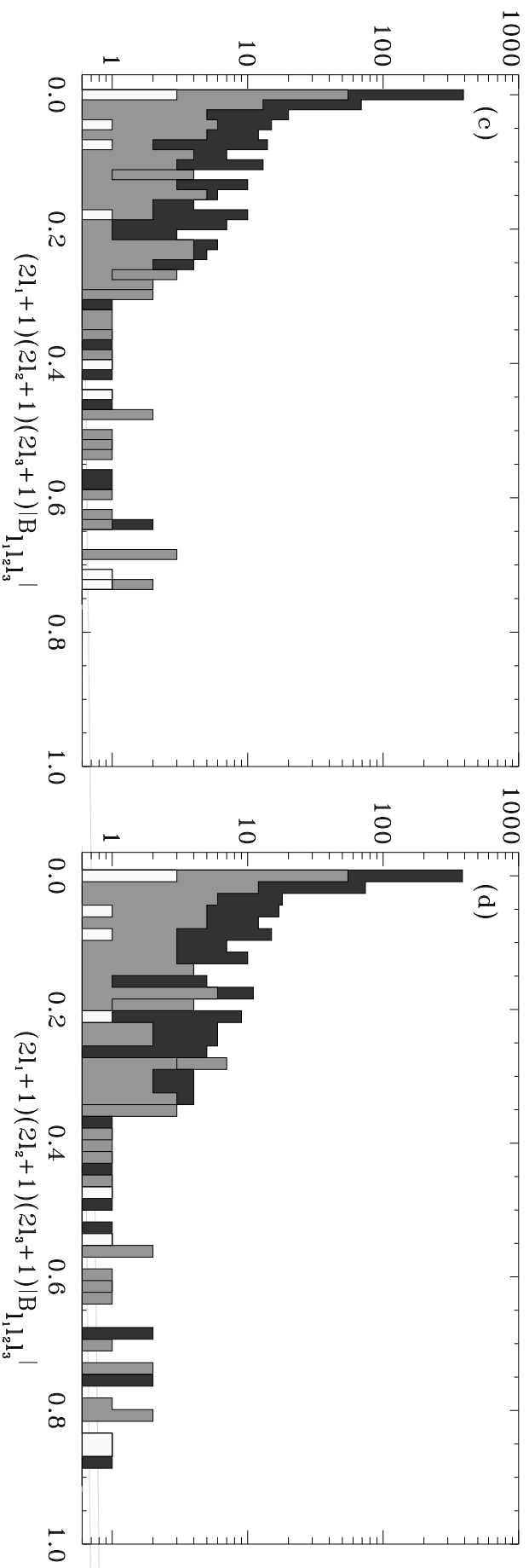
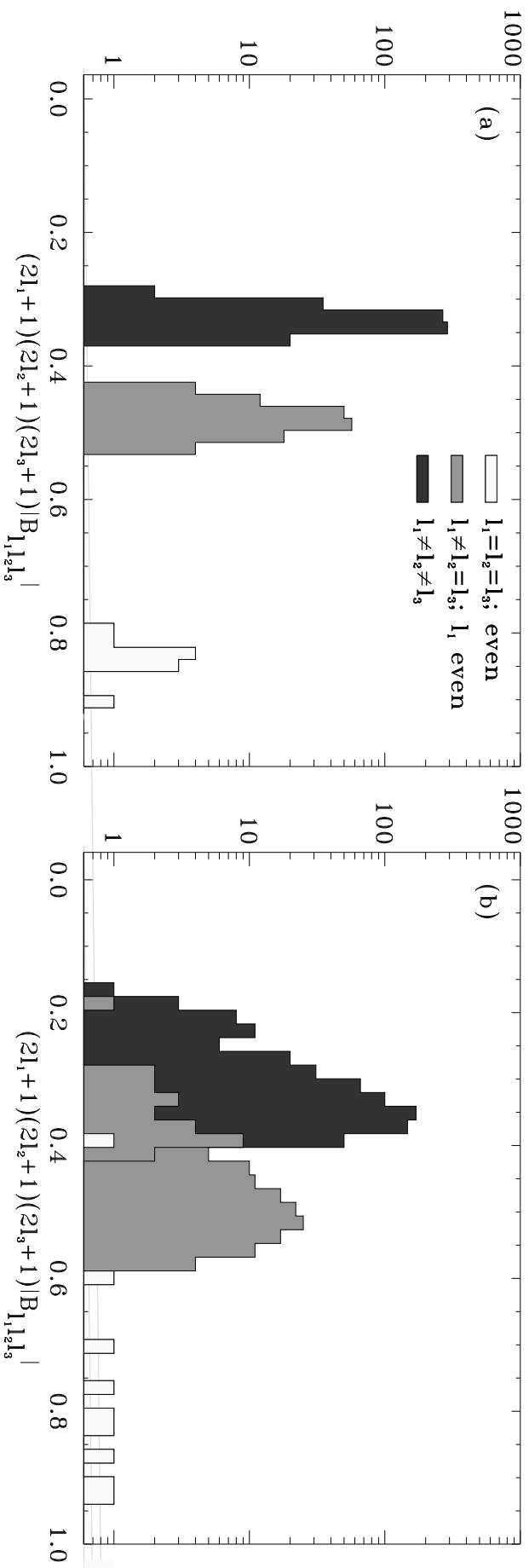
Fig. 6.— The distribution function $dN_2(\alpha)\Delta\alpha$ for partially-wound events. The smooth curve is the fitted χ_4^2 distribution with 4 degrees of freedom.

Table 1. Distribution of Model Identifications

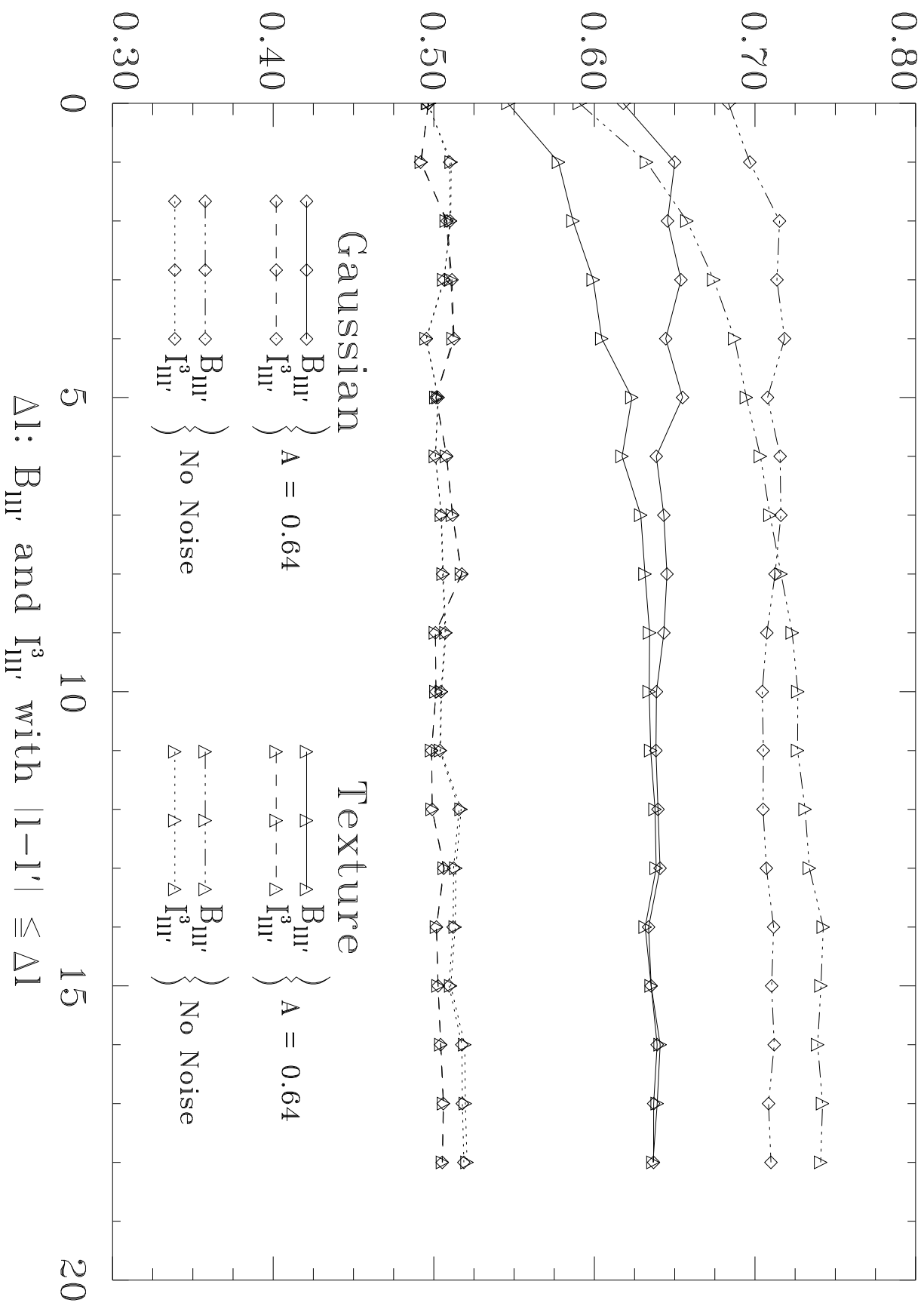
Input Model	Identified as	
	Gaussian	Texture
Gaussian	990	451
Texture	704	845

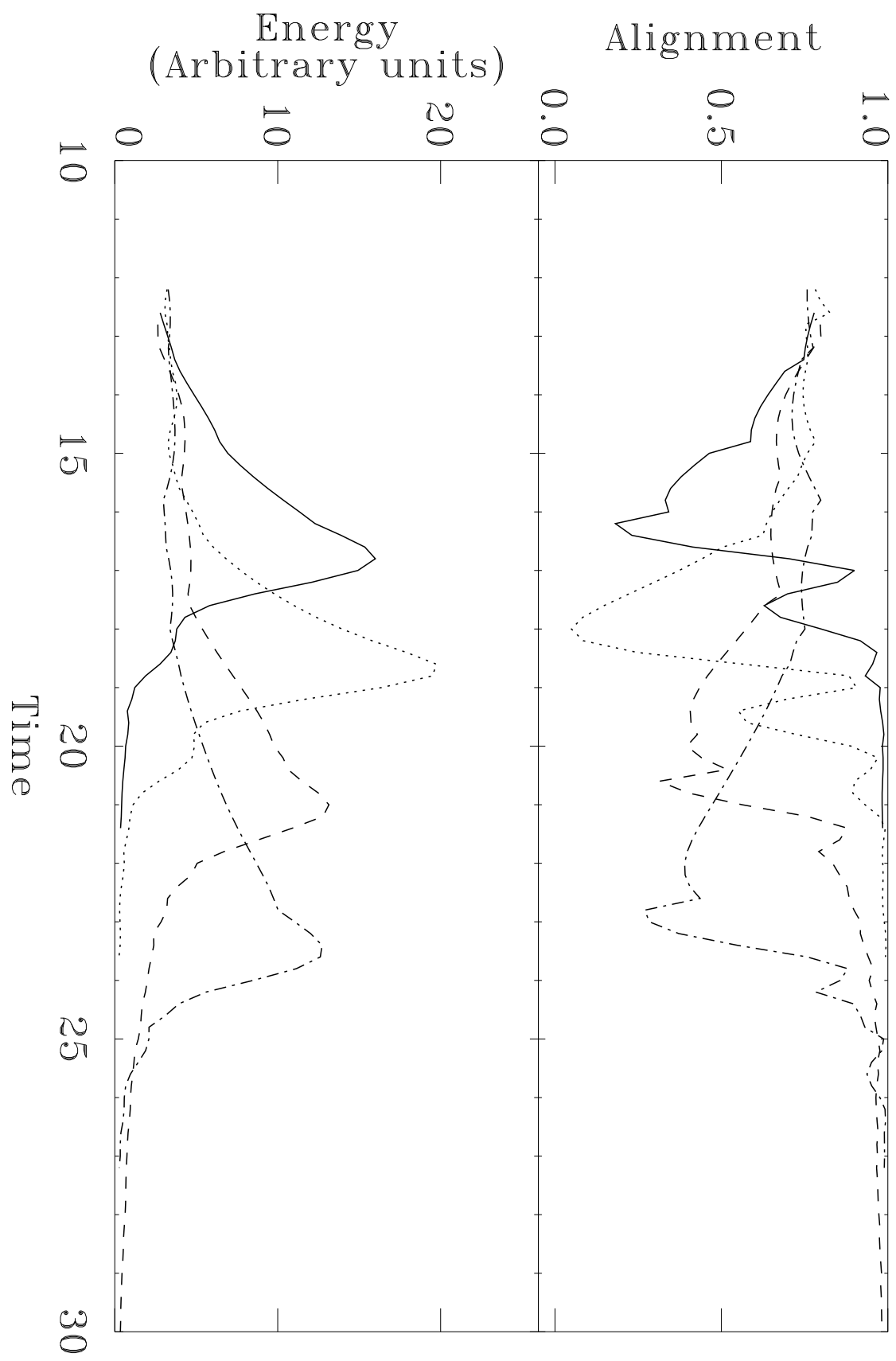
Table 2. Statistical Power of Analyzed Tests

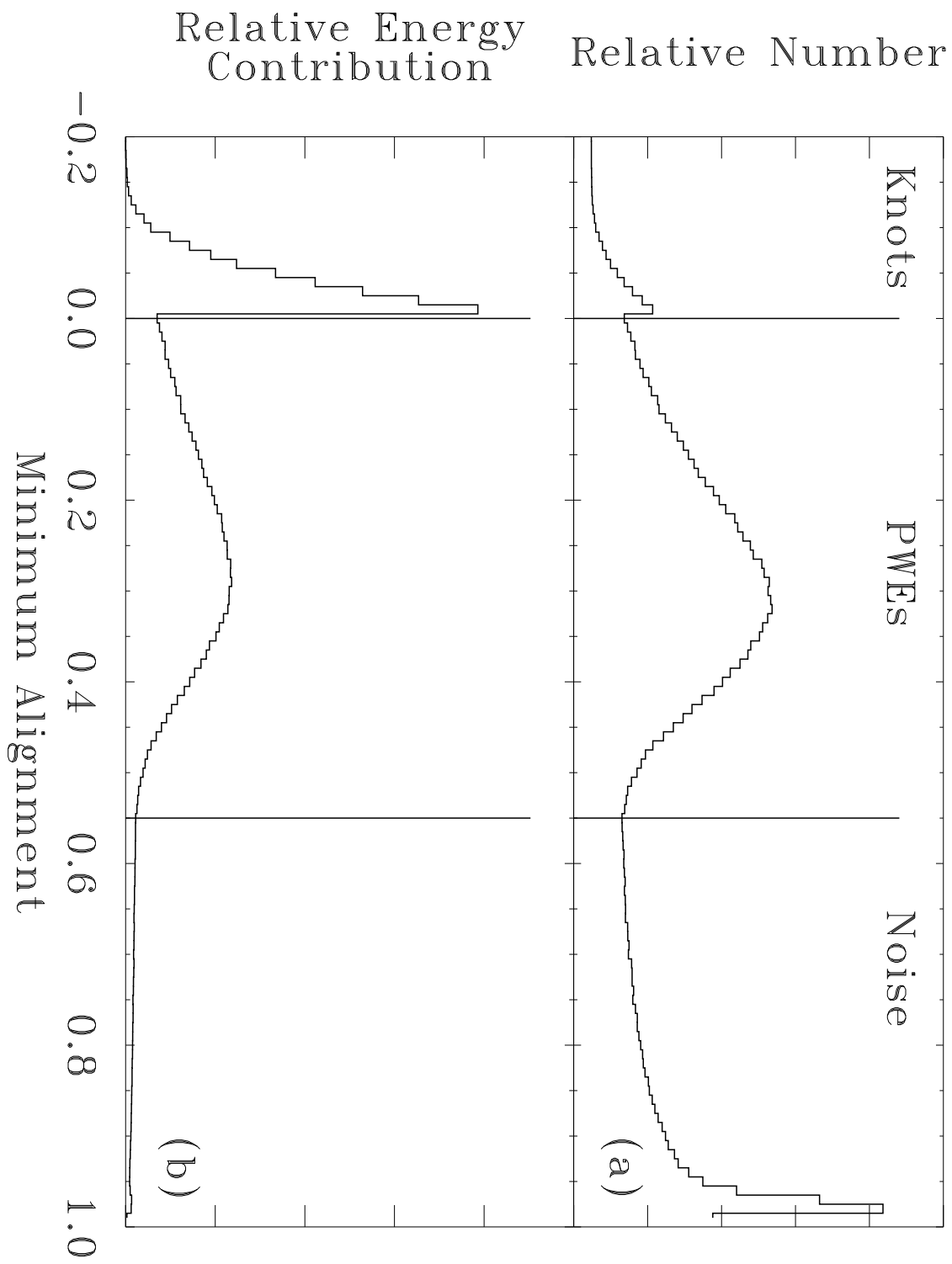
Statistic	Noise Map	Amplitude	Galaxy Cut	Probability Right	
				Gaussian	Texture
Genus	Corr	$A_{\text{fit}} = 0.64$	Template	58	65
Genus	Comb	$A_{\text{fit}} = 0.66$	Template	51	54
Extrema	Corr	$A_{\text{fit}} = 0.61$	Template	61	66
Extrema	Comb	$A_{\text{fit}} = 0.72$	Template	54	55
Bispectrum with varying Galaxy Cut					
Genus	Corr	$A = 0.64$	$b \leq 14^0$	63	62
B_{ll}	Corr	$A = 0.64$	$b \leq 14^0$	52	51
I_{ll}^3	Corr	$A = 0.64$	$b \leq 14^0$	51	51
Genus	Corr	$A = 0.64$	None	68	67
B_{ll}	Corr	$A = 0.64$	None	64	64
I_{ll}^3	Corr	$A = 0.64$	None	51	51
Bispectrum with and without Off-Diagonal Terms, with Noise					
B_{ll}	Corr	$A = 0.64$	None	62	55
B_{ll}	Corr	$A = 0.64$	None	64	64
I_{ll}^3	Corr	$A = 0.64$	None	50	50
I_{ll}^3	Corr	$A = 0.64$	None	51	51
Bispectrum with and without Off-Diagonal Terms, Noiseless					
B_{ll}	None		None	68	59
B_{ll}	None		None	71	74
I_{ll}^3	None		None	50	50
I_{ll}^3	None		None	52	52



Probability Right







Distribution $dN(\alpha)\Delta\alpha$

